Continuum kinetic modeling of the tokamak plasma edge

M. A. Dorf, M. R. Dorr, J. A. Hittinger, R. H. Cohen, and T. D. Rognlien

Citation: Physics of Plasmas **23**, 056102 (2016);
View online: https://doi.org/10.1063/1.4943106
View Table of Contents: http://aip.scitation.org/toc/php/23/5
Published by the American Institute of Physics

Continuum kinetic modeling of the tokamak plasma edge

M. A. Dorf,[1,a)] M. R. Dorr,[1] J. A. Hittinger,[1] R. H. Cohen,[2] and T. D. Rognlien[1]
[1]*Lawrence Livermore National Laboratory, Livermore, California 94550, USA*
[2]*CompX, P.O. Box 2672, Del Mar, California 92014, USA*

(Received 18 November 2015; accepted 15 December 2015; published online 10 March 2016)

The first 4D (axisymmetric) high-order continuum gyrokinetic transport simulations that span the magnetic separatrix of a tokamak are presented. The modeling is performed with the COGENT code, which is distinguished by fourth-order finite-volume discretization combined with mapped multi-block grid technology to handle the strong anisotropy of plasma transport and the complex X-point divertor geometry with high accuracy. The calculations take into account the effects of fully nonlinear Fokker-Plank collisions, electrostatic potential variations, and anomalous radial transport. Topics discussed include: (a) ion orbit loss and the associated toroidal rotation and (b) edge plasma relaxation in the presence of anomalous radial transport. © *2016 AIP Publishing LLC*.
[http://dx.doi.org/10.1063/1.4943106]

I. INTRODUCTION

As magnetic fusion devices operate at higher power, it is increasingly important to achieve an improved theoretical understanding of edge plasma transport in order to control core energy confinement and to maintain the necessary limit on plasma heat flux to surrounding material components. The problem provides substantial challenges for analytical or numerical analysis due to (a) complex magnetic geometry including both open and closed magnetic field lines **B**, (b) steep radial gradients comparable to ion drift-orbit excursions, and (c) a variation in the collision mean-free path along **B** from long to short compared to the magnetic connection length. A kinetic equation that includes a detailed collision operator must be solved to capture these key features. Furthermore, because it is important to simulate both short timescale turbulence and long timescale transport, this is also a multiscale temporal problem. Motivated in part by the success of continuum kinetic codes for core physics[1,2] and in part by their potential for high accuracy, we have been developing such a code, called COGENT, for the edge. One central feature of such a model that poses a challenge is the presence of the magnetic separatrix within the simulation domain. In more detail, strong anisotropy of plasma transport, which is much faster along the field lines than in the perpendicular direction, motivates the use of the flux-aligned coordinate surfaces for continuum methods that discretize a kinetic equation for the particle distribution function, f, on a phase-space grid. However, such coordinate surfaces have diverging metric coefficients at the X-point of the magnetic separatrix, thereby introducing a challenge for high-order accurate discretization methods. In contrast to the continuum approach, particle-in-cell (PIC) methods use macroparticles to integrate along the characteristic of a kinetic equation, and therefore are much less sensitive to the presence of the X-point, where a particle's gyro-center velocity is well defined. Such PIC models have been extensively used in the last decade for modeling the tokamak edge.[3–6] On the other hand, PIC codes may require a very large number of particles to reduce numerical noise in edge-plasma simulations to a tolerable level, where deviations from the background distribution are large and the full-f approach is required. Therefore, it is of great practical importance to develop a high-order gyrokinetic continuum code that can handle the complexity of tokamak divertor geometry with high accuracy. As we move forward, such continuum models should be compared with codes based on PIC methods.

The present work reports on the development and application of the first 4th-order finite-volume (continuum) gyrokinetic code COGENT that simulates plasma transport in a divertor geometry. Such progress in edge plasma modeling was facilitated by the recent advances in computational methods associated with the development of a high-order mapped-multiblock finite-volume discretization schemes.[7–9] These numerical algorithms employ multiple grid blocks (grid patches) to represent the magnetic geometry structure of a diverted tokamak. The coordinate surfaces of each block are aligned to magnetic flux surface everywhere except near the X-point, and a high-order interpolation is used to provide data communication in the region where the grid blocks overlap.

The present version of the COGENT code models a nonlinear axisymmetric 4D $(\mathbf{R}, v_{\|}, \mu)$ gyrokinetic equation coupled to the long-wavelength limit of the gyro-Poisson equation. Here, **R** is the particle gyro-center coordinate in the poloidal plane, and $v_{\|}$ and μ are the gyro-center velocity parallel to the magnetic field and the magnetic moment, respectively. The code has a number of collision models, ranging from the simple Krook operator to the fully nonlinear Fokker-Plank (FP) operator.[10,11] Previously, COGENT models and algorithms have been extensively verified with the annular-geometry version of the code in simulations of neoclassical transport and collisionless relaxation of geodesic acoustic modes.[12,13] Here, we report on the first results of cross-separatrix transport simulations obtained with the divertor-version of the code, which includes both the pedestal and the scrape-off-layer (SOL) regions. In particular, we apply COGENT to the problem of ion orbit loss and the

Note: Paper GI2 2, Bull. Am. Phys. Soc. **60**, 109 (2015).
[a)]Invited speaker.

associated toroidal rotation driven by this mechanism. The "intrinsic" toroidal rotation (i.e., that occurs in the absence of any auxiliary injected torque) has been routinely observed in a tokamak edge in the direction of the plasma current, I_p,[14] and the ion orbit losses are considered as one of the plausible underlying mechanisms for this phenomenon.[15,16] Another topic presented concerns relaxation of the edge plasma in the presence of anomalous radial transport. We note that some aspects of the cross-separatrix plasma transport have been previously investigated with COGENT's predecessor—the TEMPEST code.[17] While providing important insights, the earlier analysis did not take into account the effects of electric fields and fully nonlinear Fokker-Planck collisions. Also, the simulations employed computational grids flux-aligned in the entire simulation domain including the X-point region, which led to a degraded accuracy (i.e., lower order) of the discretization schemes.

This paper is organized as follows: The simulation model is summarized in Sec. II. In Sec. III, the code is verified against an analytical calculation of the collisionless ion orbit loss. The orbit-loss-driven toroidal rotation and the effects of fully nonlinear Fokker-Plank collisions and electrostatic potential variations are investigated in Secs. IV and V, respectively. Finally, in Sec. VI we present an illustrative simulation of edge plasma relaxation taking into account the effects of anomalous radial transport, ion-ion FP collisions, and the self-consistent evolution of a radial electric field.

II. SIMULATION MODEL

The present version of the COGENT code solves an axisymmetric 4D gyrokinetic equation for a gyro-center distribution function $f_\alpha(\mathbf{R}, v_\parallel, \mu, t)$ given by[18]

$$\frac{\partial B^*_{\parallel\alpha} f_\alpha}{\partial t} + \nabla_{\mathbf{R}} \cdot \left(\dot{\mathbf{R}}_\alpha B^*_{\parallel\alpha} f_\alpha\right) + \frac{\partial}{\partial v_\parallel}\left(\dot{v}_\parallel B^*_{\parallel\alpha} f_\alpha\right) = C_\alpha\left[B^*_{\parallel\alpha} f_\alpha\right]. \tag{1}$$

Here, α denotes the particle species, $\mathbf{R}$ is the gyro-center coordinate in the poloidal plane, $\nabla_{\mathbf{R}}$ is the gradient with respect to $\mathbf{R}$, and the gyro-center velocity $\dot{\mathbf{R}}$ is given by

$$\dot{\mathbf{R}}_\alpha = \frac{1}{B^*_{\parallel\alpha}}\left[v_\parallel \mathbf{B}^*_\alpha + \frac{1}{Z_\alpha e}\mathbf{b} \times (Z_\alpha e \nabla\Phi + \mu \nabla B)\right]. \tag{2}$$

The evolution of the gyro-center parallel velocity is specified by

$$\dot{v}_\parallel = -\frac{1}{m_\alpha B^*_{\parallel\alpha}} \mathbf{B}^*_\alpha \cdot (Z_\alpha e \nabla\Phi + \mu \nabla B), \tag{3}$$

where m_α and Z_α are the species mass and charge state, respectively, e is the fundamental charge, $\mathbf{B}(\mathbf{R}) = B\mathbf{b}$ is the magnetic field with $\mathbf{b}$ denoting the unit vector along the field, $\mathbf{B}^*_\alpha(\mathbf{R}, v_\parallel) \equiv \mathbf{B} + (m_\alpha v_\parallel / Z_\alpha e)\nabla \times \mathbf{b}$, $B^*_{\parallel\alpha}(\mathbf{R}, v_\parallel) \equiv \mathbf{B}^*_\alpha \cdot \mathbf{b}$, and the long wavelength (drift-kinetic) limit, $k_\perp \rho_\alpha \ll 1$, is presently assumed to describe electrostatic potential variations, $\Phi(\mathbf{R}, t)$, and collision models, $C_\alpha[f_\alpha]$. Here, $\rho_\alpha = V_{T,\alpha}/\Omega_\alpha$ is the particle thermal gyroradius, $V_{T,\alpha} = \sqrt{2T_\alpha/m_\alpha}$ is the thermal velocity, $\Omega_\alpha = Z_\alpha eB/(m_\alpha c)$ is the cyclotron frequency, and $k_\perp^{-1}$ represents the characteristic length-scale for variations in the electrostatic potential and distribution function perturbations. The implementation and testing of the corresponding long-wavelength 2D gyro-Poisson equation coupled to the Boltzmann model for electrons is described in our previous works[12,13] that focused on modeling the closed field line pedestal region. While recognizing the importance of poloidal potential variations in edge plasmas, here we restrict our initial studies of cross-separatrix transport to include only the effects of a radial electric field, E_r. The corresponding simplified flux-surface average model for E_r is described in detail in Sec. V. The collisional models available in the COGENT code include a simple drag-diffusion operator in parallel velocity,[10] Krook collisions, Lorentz collisions, linearized model Fokker-Planck collision operator conserving momentum and energy,[12] and the full nonlinear Fokker-Plank operator.[11] Finally, model terms describing the effects of anomalous radial transport can be added in Eq. (1) as discussed in detail in Sec. VI.

The COGENT code has various options for the magnetic field geometry. In particular, the Miller model[19] is available in the closed flux surface version of the code to describe the core region, and the divertor version of code supports a single-null geometry with closed and open magnetic field lines. For simplicity and for the purposes of code verification, here we adopt the following model single-null magnetic geometry (Fig. 1) that is roughly consistent with the parameters characteristic of the DIII-D tokamak. The normalized poloidal flux function is specified by

$$\psi_N(R,Z) = \cos\left[c_1(R-R_0)/L_N\right] + c_2 \sin\left[(Z-Z_0)/L_N\right] - c_3(Z-Z_0)/L_N, \tag{4}$$

for $Z > Z_x$, and it is symmetric around the plane $Z = Z_x$, i.e., $\psi_N(R, Z) = \psi_N(R, 2Z_x - Z)$. Here, R and Z are the radial

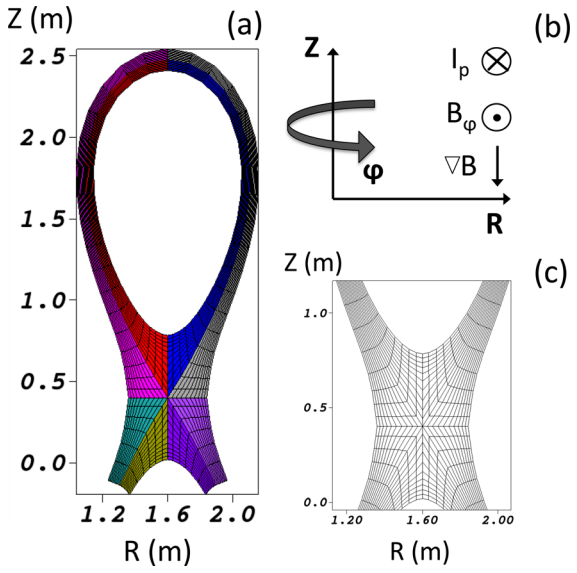

FIG. 1. Schematic of the COGENT spatial grid and coordinate system. The frames show (a) the multiblock grid structure, where blocks are distinguished by color; (b) the coordinate system and directions of the plasma current, I_p, and the toroidal magnetic field, B_ϕ; and (c) zoom-in on the grid structure near the X-point.

and vertical coordinates, respectively, $Z_x = Z_0 - L_N \arccos(c_3/c_2)$ corresponds to the vertical position of the X-point, $c_1 = 1.2$, $c_2 = 0.9$, and $c_3 = 0.7$ are the constant shape factors, $L_N = 1\,\text{m}$ is a normalizing spatial scale, $R_0 = 1.6\,\text{m}$ is the major radius coordinate corresponding to the location of the magnetic axis, and $Z_0 = 0.4\text{m} + L_N \arccos(c_3/c_2)$ is a constant vertical shift adopted for visualization purposes. For the simulations reported, the radial width of the open and closed field line regions is taken to be $\Delta_R = 6.7\,\text{cm}$ as measured at the top of the tokamak. The poloidal $(B_R,\ B_Z)$ and toroidal (B_ϕ) components of the magnetic field are determined from

$$B_R = -\frac{1}{R}\frac{\partial\psi}{\partial Z},\ B_Z = \frac{1}{R}\frac{\partial\psi}{\partial R},\quad B_\phi = -I/R, \tag{5}$$

where the poloidal flux is given by

$$\psi = \psi_N \bar{B}_\theta R_{mp}\left(\sqrt{[\partial\psi_N/\partial R]^2 + [\partial\psi_N/\partial Z]^2}\right)^{-1}\Big|_{R_{mp},\,Z_{mp}}. \tag{6}$$

Here, $\bar{B}_\theta = 0.17\,\text{T}$ is the magnitude of the poloidal magnetic field at the intersection of the separatrix and the outboard midplane corresponding to $R_{mp} = 2.107\,\text{m}$ and $Z_{mp} = Z_0 + L_N \arccos(c_3/c_2) = 1.76\,\text{m}$, and the directions of the coordinate system unit vectors are given by $[\boldsymbol{e}_R \times \boldsymbol{e}_\phi] = \boldsymbol{e}_Z$ [see Fig. 1(b)]. To describe the toroidal magnetic field, we take $I = 3.5\ \text{T}\cdot\text{m}$, except for the simulations reported in Sec. V [in Figs. 8 and 9], where $I = 0.5\ \text{T}\cdot\text{m}$ is used. Finally, for all simulations reported, a single deuterium ion species is considered, i.e., $Z_i = 1$ and $m_i = 2m_p$, where m_p denotes the proton mass.

As mentioned earlier, continuum methods solve a kinetic equation [e.g., Eq. (1)] by discretizing it on a computational phase-space grid. Due to strong anisotropy of plasma transport, it is highly advantageous to use a computational grid that is aligned with the magnetic flux surfaces. However, for the case of a divertor geometry, such a coordinate system has diverging metric coefficients at the X-point (as evidenced by the kink in the poloidal magnetic field), which can significantly degrade the convergence properties of a numerical scheme. In order to take advantage of highly efficient high-order (here, 4th-order) finite-volume algorithms,[7] the COGENT code adopts the *mapped multiblock* approach,[9] in which the spatial simulation domain is divided into logical blocks [Fig. 1(a)]. The computational grid of each block is flux-aligned everywhere excluding a small vicinity of the X-point, where the grid is smoothly extended [Fig. 1(c)]. Note that arbitrary geometry of the radial grid lines, $\theta(R,Z) = const$, is allowed and that local grid orthogonality is not assumed. The kinetic equation is solved in each block (with the use of its own computational grid) subject to high-accuracy coupling across the block boundaries. A detailed description of the method and its application to the case of X-point geometry is discussed in detail in Ref. 9. It is important to note that poloidal/radial transport anisotropy becomes less pronounced near the X-point, where the de-alignment from the magnetic flux surfaces takes place. Indeed, the poloidal projection of the ion parallel streaming velocity, $V_\theta \sim V_{Ti}(B_\theta/B)$, and the vertical component of the magnetic drift velocity, $V_{\nabla B} \sim V_{Ti}^2/(\Omega_i R)$, become comparable as the poloidal magnetic field goes to zero at the X-point. Therefore, the loss of flux-alignment in a small vicinity of the X-point that occurs in the adopted multiblock approach should not, in principle, degrade the code performance.

III. PROMPT ION ORBIT LOSSES: VERIFICATION TEST

The analysis is begun with a simple test case of collisionless ion dynamics in the absence of electric fields. While overly simplified, the model describes prompt orbit losses and can elucidate the effect of intrinsic toroidal rotation due to this mechanism. Furthermore, this model allows for analytical calculation of the loss-cone boundaries, which is used here for verification purposes. For the present test case, the initial Maxwellian distribution with spatially uniform density, $n_0 = 10^{19}\,\text{m}^{-3}$, and temperature, $T_0 = 900\,\text{eV}$, profiles, and a zero parallel flow velocity is subject to collisionless relaxation until the orbit-loss regions are depleted. The boundary condition at the inner radial boundary (of the core region) is taken to be the initial Maxwellian distribution, and all other boundaries, i.e., the divertor plates and outer radial boundaries, are assumed to absorb particles. Figure 2(a) shows the velocity phase space obtained at the outboard midplane, 3.2 cm inside the last closed flux surface (LCFS), i.e., the magnetic separatrix. The evident loss-cone is associated with the prompt ion orbit losses. Integrated over the velocity space, such a distribution yields a non-trivial toroidal flow velocity in the direction of the plasma current (co-I_p).

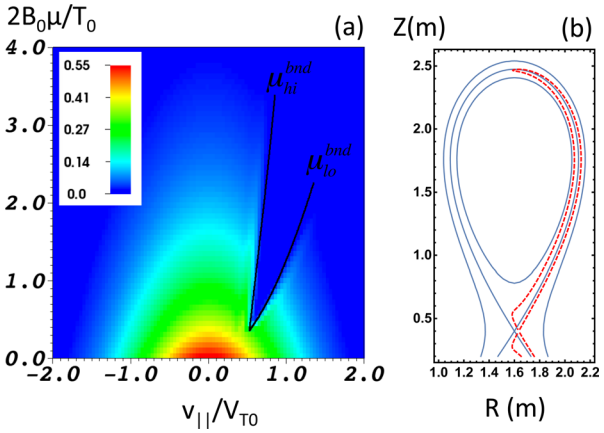

FIG. 2. Collisionless relaxation of an ion Maxwellian distribution with uniform density, $n_0 = 10^{19}\,\text{m}^{-3}$, and temperature, $T_0 = 900\,\text{eV}$, profiles, in the absence of electric fields. Frame (a) shows the velocity phase-space slice of the ion distribution (in arbitrary units) obtained at $R = 2.075\,\text{m}$ and $Z = 1.76\,\text{m}$, which corresponds to the point on the outer midplane, 3.2 cm inside the magnetic separatrix. Bold curves show the analytical solution for the loss-cone boundaries [Eq. (8)]. The spatial grid resolution corresponds to $[N_\psi = 32,\ N_\theta = 128]$, $[N_\psi = 32,\ N_\theta = 170]$, and $[N_\psi = 32,\ N_\theta = 42]$ in the CORE, SOL, and PF regions, respectively. The velocity grid is $[N_{v_\parallel} = 96,\ N_\mu = 66]$, and the maximum values of $|v_\parallel|$ and μ correspond to $v_\parallel^{max}/V_{T0} = 2.0$, $B_0\mu_{max}/T_0 = 2.3$, where $B_0 = 1.0\,\text{T}$, $V_{T0} = \sqrt{2T_0/m_i}$, and $m_i = 2$. The initial Maxwellian distribution is used to specify the inflow fluxes at the inner radial boundary, and all other boundaries are assumed to absorb particles. Frame (b) shows the ion "separatrix" trajectory obtained for to $v_\parallel/V_{T0} = 0.68$, $2B_0\mu/T_0 = 1.78$, which corresponds to the "high-μ" boundary of the loss-cone region.

The COGENT simulations show excellent agreement with the analytical calculation of the loss cone boundaries [Fig. 2(a)], which is obtained as follows: For a given value of the parallel velocity, the value of magnetic moment at the "high-μ" boundary of the loss-cone region, $\mu_{bnd}^{hi}(\mathrm{v}_\parallel)$ [see Fig. 2(a)], corresponds to the "separatrix" particle trajectory shown in Fig. 2(b). Particles launched from the outboard midplane with the same value of the parallel velocity, $\mathrm{v}_\parallel$, have confined orbits for $\mu > \mu_{lo}^{bnd}$, and are lost to the divertor plates for $\mu_{lo}^{bnd} < \mu < \mu_{hi}^{bnd}$. The "low-$\mu$" boundary of the loss-cone region, $\mu_{bnd}^{lo}(\mathrm{v}_\parallel)$, corresponds to the usual "trapped–passing" boundary that separates banana and passing orbits, where particles launched with $\mu < \mu_{hi}^{bnd}$ have confined (passing) orbits. The "low-μ" and "high-μ" boundaries intersect at μ_{min} and $\mathrm{v}_\parallel^{min}$, which determines the minimal particle energy $E_{min} = m_i(\mathrm{v}_\parallel^{min})^2/2 + \mu_{min}B$ corresponding to a lost orbit. Also note that, for higher particle energies, the "low-μ" boundary rolls over toward the $\mathrm{v}_\parallel$-axis (see Refs. 4 and 15 for details). The analysis of that part of the loss-cone boundary is outside the scope of the present verification test.

Using the conservation of particle energy, $E = m_i\mathrm{v}_\parallel^2/2 + \mu B$, magnetic moment, μ, and angular momentum, $p_\phi = m_i R\mathrm{v}_\parallel B_\phi/B + (e/c)\psi$, the (R,Z) trajectory of a particle launched from the location $R = R_0$, $Z = Z_0$, with $\mathrm{v}_\parallel = \mathrm{v}_{\parallel,0}$, $\mu = \mu_0$, is specified by the following equation:

$$T_p(R,Z) \equiv mR_0\mathrm{v}_{\parallel,0}\frac{B_\phi(R_0,Z_0)}{B(R_0,Z_0)} + \frac{e}{c}[\psi(R_0,Z_0) - \psi(R,Z)] \pm m_i R\frac{B_\phi(R,Z)}{B(R,Z)}\left(\mathrm{v}_{\parallel,0}^2 + \frac{2}{m_i}\mu_0[B(R_0,Z_0) - B(R,Z)]\right)^{1/2} = 0. \quad (7)$$

The "high-μ" boundary, $\mu_{bnd}^{hi}(\mathrm{v}_\parallel)$, can now be found by making use of the singularity condition at the X-point of the separatrix particle trajectory shown in Fig. 2(b), i.e.,

$$\left.\frac{\partial T_p(R,Z)}{\partial R}\right|_{R_{x_p},Z_{x_p}} = 0, \quad \left.\frac{\partial T_p(R,Z)}{\partial Z}\right|_{R_{x_p},Z_{x_p}} = 0, \quad T_p\left(R_{x_p},Z_{x_p}\right) = 0, \quad (8)$$

where R_{x_p} and Z_{x_p} are the radial and vertical coordinates of the X-point, respectively. The solution to system (8) yields the "high-μ" boundary of the loss-cone for the configuration point $R = R_0$, $Z = Z_0$. The "low-μ" boundary (here, the trapped-passing boundary) can be found from

$$\left.\frac{\partial T_p(R,Z)}{\partial R}\right|_{R_{tp},Z_{mp}} = 0, \quad T_p(R_{tp},Z_{mp}) = 0, \quad (9)$$

where the first equation in system (9) corresponds to the condition that the vertical component of the particle velocity vanishes at the inboard midplane, i.e., $Z = Z_{mp}$, and R_{tp} denotes the radial particle coordinate at this turning point. Finally, the minimal energy point $(\mu_{min}, \mathrm{v}_\parallel^{min})$ can be determined by requiring that Eqs. (8) and (9) are simultaneously satisfied for $\mu_0 = \mu_{min}$ and $\mathrm{v}_{\parallel,0} = \mathrm{v}_\parallel^{min}$.

IV. TOROIDAL ROTATION AND THE EFFECTS OF COLLISIONS

Ion dynamics and generation of plasma toroidal rotation are now discussed in more detail, including the effects of the fully nonlinear ion-ion Fokker-Plank collision model. As an illustrative example, we consider relaxation of an initial Maxwellian distribution with spatially uniform density, $n_0 = 10^{19}\,\mathrm{m}^{-3}$, and temperature, $T_0 = 300\,\mathrm{eV}$, and a zero parallel flow velocity. These values of the plasma density and temperature are consistent with the near-separatrix parameters characteristic of the DIII-D tokamak (e.g., see Ref. 14). The same Maxwellian distribution is used to specify inflow fluxes at the inner radial core boundary, and all other boundaries (i.e., the divertor plates and outer radial boundaries) are assumed to absorb particles. The spatial grid resolution is given by $[N_\psi = 32,\ N_\theta = 72]$, $[N_\psi = 32, N_\theta = 96]$, and $[N_\psi = 32, N_\theta = 24]$ in the core, SOL, and private flux (PF) regions, respectively. The velocity grid is $[N_{\mathrm{v}_\parallel} = 72, N_\mu = 48]$, and the total number of cells corresponds to 21×10^6. Here, $N_{\psi,\theta,\mathrm{v}_\parallel,\mu}$ correspond to the number of cells in the directions of the radial coordinate, poloidal coordinate, parallel velocity, and magnetic moment, respectively. The same grid resolution is used for all simulations that follow, expect for those discussed in Sec. VI. The code performance scales well with the number of processors, and it takes approximately 2000 CPU hours [e.g., $4\,\mathrm{h} \times 400$ processors] to simulate 1 ms of ion dynamics on the Edison cluster of the NERSC computing system.[20]

We begin with analysis of the collisionless case [see Figs. 3(a) and 3(c)]. Figure 3(a) shows the ion-species density after 2.5 ms, which corresponds to 83 transit time periods of a thermal ion defined as, $\tau_{tr} = (\bar{B}_\phi/\bar{B}_\theta)(\bar{a}/V_{T0}) = 30\,\mu\mathrm{s}$. Here, the minor radius, $\bar{a} = R_{mp} - R_0$, and the magnetic field components correspond to the intersection of the outboard midplane and the separatrix, and $V_{T0} = \sqrt{2T_0/m_i}$. It is readily seen that the ion density is significantly depleted on open field lines except for the regions (at the outboard mid-plane and at the inboard side of $Z = Z_x$ plane), where the magnetic-well effect provides confinement of ions with a sufficiently large ratio $|\mathrm{v}_\perp/\mathrm{v}_\parallel|$. Figure 3(c) illustrates the formation of the loss-cone region in the ion velocity phase-space at the outboard midplane. Note that although the grid resolution used for the simulations in this section is coarser than that of the verification test in Sec. III, there is still good agreement with the analytic calculation of the loss-cone boundaries [Fig. 3(c)]. Associated with the presence of prompt ion orbit loss is the development of the parallel ion flow velocity (Figs. 4 and 5). Note that $B_\theta/B_\phi \sim 0.1$, so here the parallel and toroidal flow velocities are nearly the same. The time evolution of the ion parallel flow velocity is shown in Fig. 4, and its radial profile obtained along the outboard and inboard midplanes at 2.5 ms is

illustrated in Fig. 5. By analyzing Figure 5, we note the rapid decay of the parallel flow velocity toward the core of a tokamak, which corresponds to the shift of the velocity loss-cone toward a high-energy (exponentially decaying) tail of the ion distribution. Also, consistent with the arguments in Ref. 14, the parallel flows developed at the inboard midplane deep in the pedestal region are in the counter-I_p direction and much smaller than the co-I_p outboard flows. However, note that near the separatrix, the inboard parallel flows become more pronounced and can be larger than their outboard counterpart.

The collisionless results in Figs. 3(c) show that the prompt ion orbit loss can provide significant deviation from a Maxwellian distribution, and therefore the fully nonlinear FP collision operator may be needed in order to provide accurate description of collisional effects. The FP collision model has been implemented and tested in the COGENT code,[11] and it is applied here to investigate the effects of ion-ion collisions on the dynamics of ion species in a tokamak edge. For the parameters of the present illustrative example, the characteristic ion-ion collision time $\tau_{ii} = 3\sqrt{m_i T_0^3}/(4\sqrt{\pi} n_0 \lambda_{ii} e^4) \approx 1\,\text{ms}$ is much larger than the ion transit time period, $\tau_{ii} \approx 33\tau_{tr}$, corresponding to a weakly collisional regime. Here, $\lambda_{ii} = 23 - \ln\{Z_i^3 (T_0[\text{eV}])^{-3/2} (2n_0[\text{cm}^{-3}])^{1/2}\}$ is the Coulomb logarithm for ion-ion collisions.[21] The results for the ion density and velocity phase-space are shown in Figs. 3(b) and 3(d), respectively. It is readily seen that the ion density inside the magnetic wells in the SOL region is significantly depleted due to collisional scattering across the trapped-passing boundaries. Also, significant collisional repopulation of the loss cone is observed. Collisional scattering of ions into the loss-cone regions followed by their loss to the divertor plates provides a continuous loss of the angular momentum from closed field line region, as seen in Fig. 4.

A deviation of the ion distribution function from a Maxwellian function is determined by the competition between ion orbit loss, which depletes the loss-cone regions of the velocity phase-space, and the collisions, which provide the loss-cone repopulation and tend to restore a Maxwellian distribution. Figure 6 shows the normalized deviation from the local Maxwellian distribution, $\delta f_i/\max(F_M)$ computed at the same location as that used in Figs. 3(c) and 3(d). Here, $\delta f_i = (f_i - F_M)$ and F_M is the equivalent local Maxwellian distribution, which has the same density, temperature, and parallel flow velocity as the original distribution, f_i, and $\max(F_M)$ denotes its maximum value. As expected, a pronounced deviation is observed within the loss-cone region [cf. Fig. 3(c)], where the corresponding locally normalized quantity, $(f_i - F_M)/F_M$, reaches near-unity values. It is instructive to consider the applicability of a linearized collision operator, $C_L[f_i] = C_{FP}[\delta f_i, F_M] + C_{FP}[F_M, \delta f_i]$, which neglects the nonlinear correction $C_{FP}[\delta f_i, \delta f_i]$ for edge plasma modeling. That is, the linearized model assumes the scattering background to be a Maxwellian distribution, F_M, and to quantify this approximation error, one needs to compute the difference in the Rosenbluth potentials due to δf_i. While such detailed analysis is outside the scope of the present work the results in Fig. 6

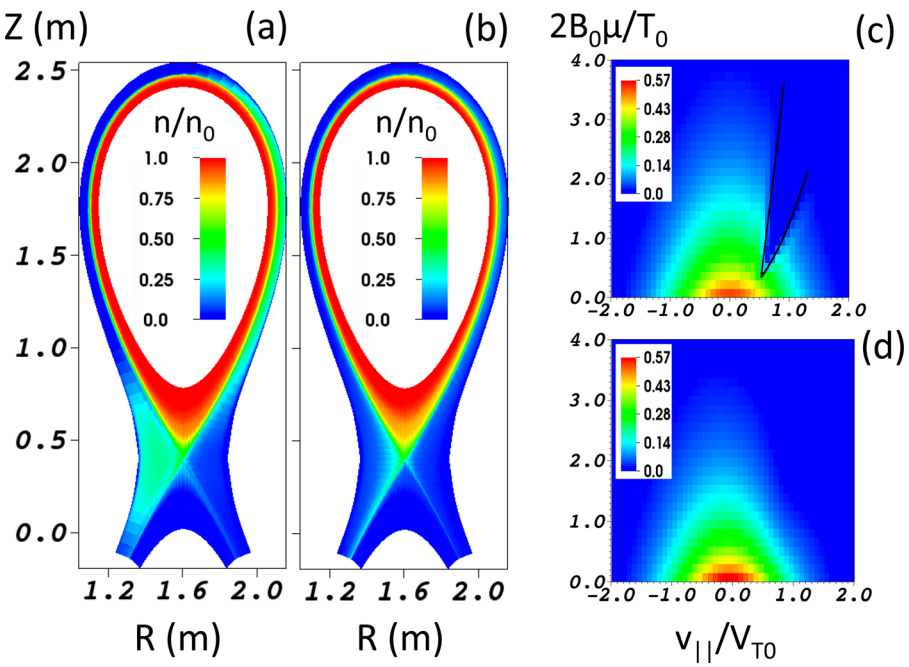

FIG. 3. Relaxation of a Maxwellian distribution with uniform density, $n_0 = 10^{19}\,\text{m}^{-3}$, and temperature, $T_0 = 300\,\text{eV}$, profiles in the absence of electric fields. The results correspond to the time instant $t = 2.5\,\text{ms}$. Frames (a), (b) and (c), (d) show the normalized ion density, n/n_0, and velocity phase-space (in arbitrary units) obtained for the Fokker-Planck collision model [(b) and (d)] and for the collisionless case [(a) and (c)], respectively. The plots in frames (c) and (d) are obtained at $R = 2.09\,\text{m}$ and $Z = 1.76\,\text{m}$, which corresponds to the point on the outer midplane, 1.7 cm inside the separatrix. The bold curves in frame (c) show the analytical solution for the loss-cone boundaries [Eq. (8)]. The spatial grid resolution corresponds to $[N_\psi = 32,\ N_\theta = 72]$, $[N_\psi = 32,\ N_\theta = 96]$, and $[N_\psi = 32,\ N_\theta = 24]$ in the CORE, SOL, and PF regions, respectively. The velocity grid is $[N_{v_\parallel} = 72,\ N_\mu = 48]$, and the maximum values of $|v_\parallel|$ and μ correspond to $v_\parallel^{max}/V_{T0} = 3.0$, $B_0\mu_{max}/T_0 = 3.5$, where $B_0 = 1.0\,\text{T}$, $V_{T0} = \sqrt{2T_0/m_i}$, and $m_i = 2$. The initial Maxwellian distribution is used to specify the inflow fluxes at the inner radial boundary, and all other boundaries are assumed to absorb particles.

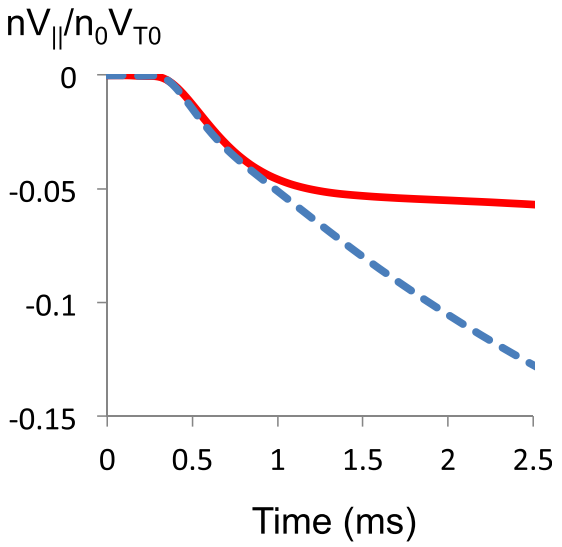

FIG. 4. Time evolution of the normalized ion parallel momentum obtained at $R = 2.09\,\mathrm{m}$, $Z = 1.76\,\mathrm{m}$ for the collisionless (solid red line) and collisional (dashed blue line) cases. The parameters of the simulation are the same as in Fig. 3.

suggest that nonlinear contributions to the collision operator can be of a non-negligible level.

V. EFFECTS OF THE RADIAL ELECTRIC FIELD

The radial electric field, E_r, can have a substantial effect on ion orbit losses and the associated development of parallel flows. We note that pronounced poloidal variations in the electrostatic potential can occur in the edge of a tokamak, especially under the H-mode conditions, where the edge gradients are large and substantial deviations from a local Maxwellian distribution can develop for ion species. The effects of poloidal electric fields will be a subject of our future studies, and here we assume that the electrostatic potential is constant on flux surfaces, i.e., $\Phi(R,Z) = \Phi(\psi)$.

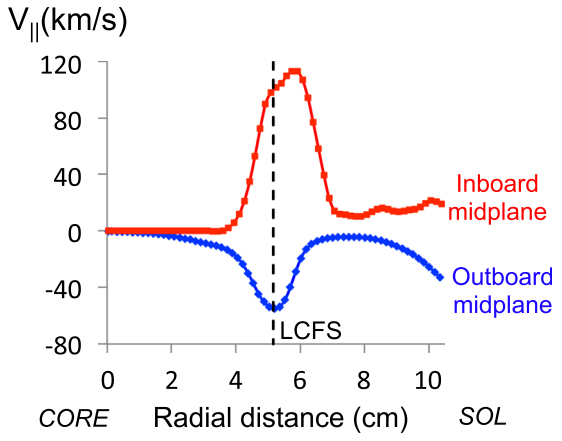

FIG. 5. Radial profiles of the parallel flow velocity computed along the inboard (red squares) and outboard (blue diamonds) midplane versus the radial distance from the inner core boundary. The outboard flows are in the co-I_p direction, and the inboard flows are in the counter-I_p direction. The results are obtained for the collisionless case and correspond to the time instant $t = 2.5\,\mathrm{ms}$. The vertical dashed line shows the location of the separatrix. The parameters of the simulation are the same as in Fig. 3.

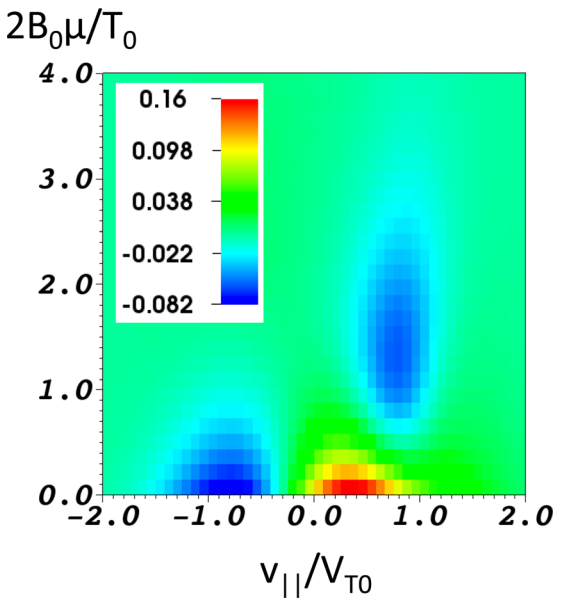

FIG. 6. Deviation of the ion distribution function from the "equivalent" Maxwellian distribution, F_M, which has the same density, parallel velocity, and temperature. Plotted is the normalized deviation $\delta f_{Ni} = (f_i - F_M)/\max(F_M)$, obtained at $R = 2.09\,\mathrm{m}$, $Z = 1.76\,\mathrm{m}$ for the collisional case at 2.5 ms. The parameters of the simulation are the same as in Fig. 3.

This simplified model still captures important physical phenomena and is also of particular importance for code verification.

First consider a simple test case that includes a fixed (i.e., not evolving in time) electric field and the ion-ion (FP) collisions. The simulations are initialized with a uniform temperature distribution, $T_0 = 300\,\mathrm{eV}$, the poloidally independent density function, $n_0(R,Z) = n_0(\psi)$ illustrated in Fig. 7(a), and a zero parallel flow velocity. The electrostatic potential distribution is chosen to be consistent with the Boltzmann equilibrium, i.e., $Z_i e n_0(\partial\Phi_0/\partial\psi) = -T_0(\partial n_0/\partial\psi)$ [Fig. 7(a)]. Also, for comparison purposes, we consider the case with a zero electric field, i.e., $\Phi_0 = 0$. The relaxation of the system is simulated for 2.5 ms, and the results are shown in Fig. 7. For the case of a zero potential, the system develops large flows across the entire core region to balance the pressure gradient force. While the pressure gradient decreases toward the separatrix, the ion orbit losses become more pronounced and enhance the parallel flow in the edge region [Fig. 7(b)]. In contrast, for the case of the initial Boltzmann equilibrium, deep in the core region the steady-state is maintained and no flows are developed. However, the presence of ion orbit loss drives the system away from the initial state toward equilibrium, which has parallel flows near the separatrix [Fig. 7(b)]. Also note that the near-separatrix parallel flows are less than those developed for the zero-E_r case. The possible explanations include the combination of (a) mitigation of the ion orbit loss due the presence of the radial electric field and (b) enhanced radial transport of the angular momentum in the regions where the distribution function substantially deviates from a local Maxwellian distribution.

We now extend the analysis to include the effects of a self-consistent radial electric field. It can be shown for the case where poloidal variations in an electrostatic potential

are neglected that the evolution of a radial electric field on closed flux surfaces is determined by[3,22]

$$\left\langle \frac{c^2 n_i m_i}{Z_i e B^2} |\nabla\psi|^2 \right\rangle \frac{\partial \Phi}{\partial t \partial \psi} = \langle \nabla\psi \cdot \mathbf{\Gamma}_i \rangle, \tag{10}$$

where

$$\mathbf{\Gamma}_i = \int (2\pi/m_i) B_\parallel^* dv_\parallel d\mu \dot{\boldsymbol{R}}_i f_i \tag{11}$$

denotes the neoclassical radial ion particle flux. The flux-surface average operator introduced in Eq. (10) is given by

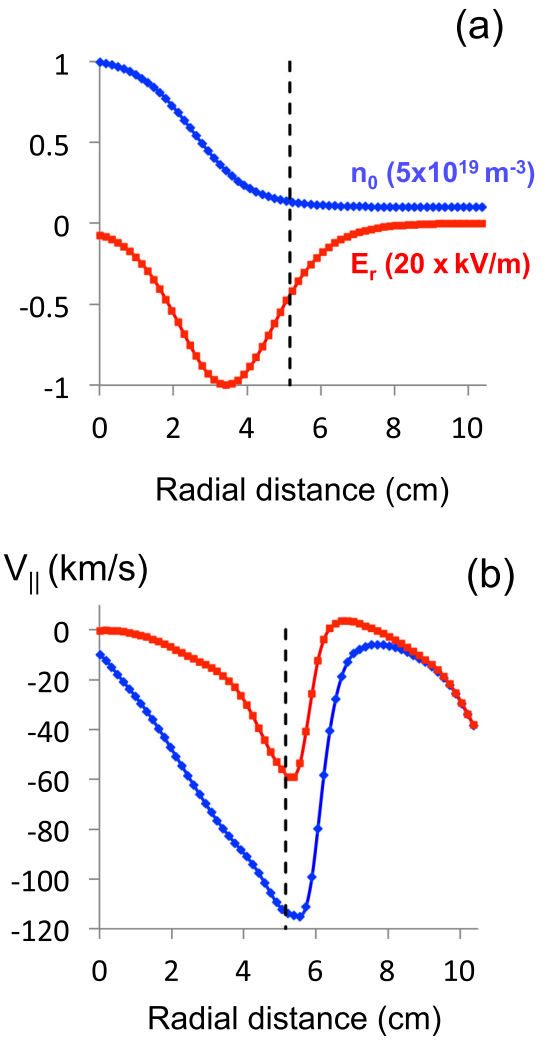

FIG. 7. Collisional relaxation of a Maxwellian distribution with non-uniform density [blue diamonds in frame (a)] and uniform temperature $T_0 = 300$ eV, profiles in the presence of a fixed radial electric field. The parallel flow velocity [frame (b)] is shown for the cases of a zero electric field (blue diamonds) and the Boltzmann equilibrium model (red squares), where the corresponding radial electric field is illustrated by the red squares in frame (a). The results in frames (a) and (b) are obtained along the outboard midplane at $t = 2.5$ ms and plotted against the radial distance from the inner core boundary. The vertical dashed lines show the location of the separatrix. The spatial grid resolution corresponds to $[N_\psi = 32,\ N_\theta = 72]$, $[N_\psi = 32,\ N_\theta = 96]$, and $[N_\psi = 32,\ N_\theta = 24]$ in the CORE, SOL, and PF regions, respectively. The velocity grid is $[N_{v_\parallel} = 72,\ N_\mu = 48]$, and the maximum values of $|v_\parallel|$ and μ correspond to $v_\parallel^{max}/V_{T0} = 3.0$, $B_0\mu_{max}/T_0 = 3.5$, where $B_0 = 1.0$ T, $V_{T0} = \sqrt{2T_0/m_i}$, and $m_i = 2$. The initial Maxwellian distribution is used to specify the inflow fluxes at the inner radial boundary, and all other boundaries are assumed to absorb particles.

$$\langle \chi \rangle = \oint \chi |\nabla\psi|^{-1} dA \Big/ \oint |\nabla\psi|^{-1} dA, \tag{12}$$

where dA is the surface element of a magnetic flux surface. Equation (10) describes the balance between the polarization and neoclassical ion currents assuming much smaller electron contributions. It is important to note that in contrast to modeling the dynamics of E_r in the core region, where the intrinsic ambipolarity of plasma transport requires higher accuracy of the gyro-kinetic equation than that of Eq. (1),[23] the presence of processes that are not intrinsically ambipolar, such as orbit loss and collisions with neutrals, can justify the use of Eq. (1) and (10)–(11) in the edge region of a tokamak.[24] The self-consistent model for the radial electric field specified by Eq. (10) has been implemented in the COGENT code for the closed field line region. The present implementation, however, computes the right-hand side of Eq. (10) neglecting the difference between the COGENT grid surfaces, ψ_C, and magnetic flux surfaces, ψ, which deviate slightly from each other near the X-point. The accuracy of such an approximation can be checked systematically by making use of less-deviated computational grids, although higher resolution may be needed to resolve rapidly varying metric coefficients near the X-point. For additional verification, a lower-order (2nd-order) version of the code has been developed for the case of the model geometry considered here (see Fig. 1). This COGENT version makes use of the analytical representation of the metric coefficients and employs a flux-aligned coordinate system for the entire simulation domain. For the simulations presented in this section, it has been verified that the difference in the flux-surface average radial particle flux [in Eq. (10)] corresponding to slight deviations of the computational grid from the magnetic flux surfaces near the X-point produces a small effect.

It follows from Eq. (10) that the ion orbit losses, which generate the outward radial particle flux, will produce a build up of the inward radial electric field. The corresponding potential barrier will act, in turn, to mitigate the losses. On open field lines, i.e., in the SOL and PF regions, the radial variations in the electrostatic potential are primarily determined by the sheath physics effects at the divertor plates, and can be roughly estimated as $\Phi(\psi) \sim T_e(\psi, \theta_{plate})/e$, where $T_e(\psi, \theta_{plate})$ is the electron temperature at the plates.[25] As the electron temperature typically increases toward the strike points, the radial electric field in the SOL region is typically directed inward, and therefore a jump in the electric field can be expected across the separatrix. Details of the potential distribution in the open field line regions are outside the scope of the present studies, and in what follows we either set the electric field to zero in the SOL and PF regions, or adopt an *ad-hoc* extrapolation model in order to avoid strong discontinuities in numerical solutions.

The effects of a self-consistent radial electric field have been tested for collisionless relaxation of a uniform Maxwellian distribution. It is observed for the parameters characteristic of the DIII-D tokamak (i.e., those used in Sec. IV) that the radial width of the pedestal structure becomes very narrow (plausibly due to the orbit squeezing effect), so that resolving the ion gyro-radius scale, ρ_i, becomes necessary.

Note that for the zero-E_r case discussed in Sec. IV, it was sufficient to resolve a much larger banana orbit width, $\Lambda_B \sim 6\rho_i$, to obtain a converged solution. In addition to a significant increase in the number of radial cells, having such a small radial cell size substantially decreases the time step needed for stability of the explicit time integration scheme employed in COGENT. In short, a stable time step for the considered collisionless advection problem is determined by the Courant constraint, i.e., $\Delta t < min(\Delta_\theta/v_\theta, \Delta_\psi/v_\psi)$, where Δ_θ and Δ_ψ are the cell sizes, and $v_\theta \sim (\bar{B}_\theta/\bar{B}_\phi)V_T$ and $v_\psi \sim (\rho_i/R_0)V_T$ are the particle streaming velocities in the poloidal and radial directions, respectively. Assuming, for simplicity, $\Delta_\psi \sim L_\psi/N$, $\Delta_\theta \sim 2\pi\bar{a}/N$, we obtain $\Delta t < N^{-1}(R_0/V_{T0})min(2\pi\bar{q}, L_\psi/\rho_i)$. Here, $\bar{q} = (\bar{B}_\phi/\bar{B}_\theta)(\bar{a}/R_0) \approx 3$ is the local magnetic safety factor at the intersection of the outboard midplane and magnetic separatrix, L_ψ is the characteristic radial scale that needs to be resolved, and N denotes the number of cells in each spatial direction. For the case of conventional neoclassical studies of a tokamak core [e.g., as in Ref. 12], the radial gradients are weak, $L_\psi \gg \Lambda_B$, and the time step is restricted by the parallel streaming. In contrast, for the case of edge plasma modeling discussed here, the time step is restricted by the radial advection across steep radial gradients, and therefore, its value decreases by the factor of $\Lambda_B/\rho_i \sim 6$ when the effects of self-consistent radial electric field are included. The severe requirements for the grid resolution and stable time step for the parameters characteristic of the DIII-D tokamak make the corresponding simulations of the idealized test case very time-consuming.

Therefore, for illustrative purposes, results are given for simulations performed for the following model parameters: $\bar{B}_\theta = 0.17\,\mathrm{T}$, $I = 0.5\,\mathrm{T}\cdot\mathrm{m}$, and $T_0 = 1000\,\mathrm{eV}$. These relaxed parameters correspond to a significantly larger value of the ion gyro-radius, $\rho_i \sim 2\,\mathrm{cm}$. Moreover, the similar values of the poloidal and toroidal magnetic field components optimize the number of time steps required to simulate the characteristic relaxation time corresponding to the ion transient time period, $\tau_{tr} = (\bar{B}_\phi/\bar{B}_\theta)(\bar{a}/V_{T0}) = 2.3\,\mu\mathrm{s}$. Note that the standard gyrokinetic model[18] used in COGENT fails to accurately describe magnetized plasmas for the case where substantial electrostatic potential variations, $\sim T_e/e$, occur on the gyro-radius length scale. However, the present simulations still illustrate the interplay between the ion orbit loss and the self-consistent generation of the radial electric field, and can also be of particular importance for code verification purposes. Figure 8 represents collisionless relaxation of the initial uniform Maxwellian distribution with $n_0 = 10^{19}\,\mathrm{m}^{-3}$, $T_0 = 1000\,\mathrm{eV}$, and a zero parallel flow velocity after $t_{sim} \sim 50 \times \tau_{tr} \sim 0.12\,\mathrm{ms}$. The simulation assumes a zero electric field on the open field lines. The outer midplane radial profiles of the electric field and parallel flow velocity are shown in Figs. 8(a) and 8(b), and the velocity phase space obtained at the outboard midplane is shown in Fig. 9(b). For comparison purposes, Figs. 8(b) and 9(a) show the parallel flow velocity profile and velocity phase-space obtained in the absence of electric fields, respectively. It is readily seen that the radial electric field mitigates both the orbit losses and development of the parallel ion flow. Also, consistent with the theoretical predictions in Ref. 26, the presence of a strong radial electric field provides a shift of the trapped-passing boundary along the $v_{||}$-axis toward the high-energy tail as seen in Fig. 9(b).

We now address the effects of a non-zero radial electric field on open field lines, for which ad-hoc models are

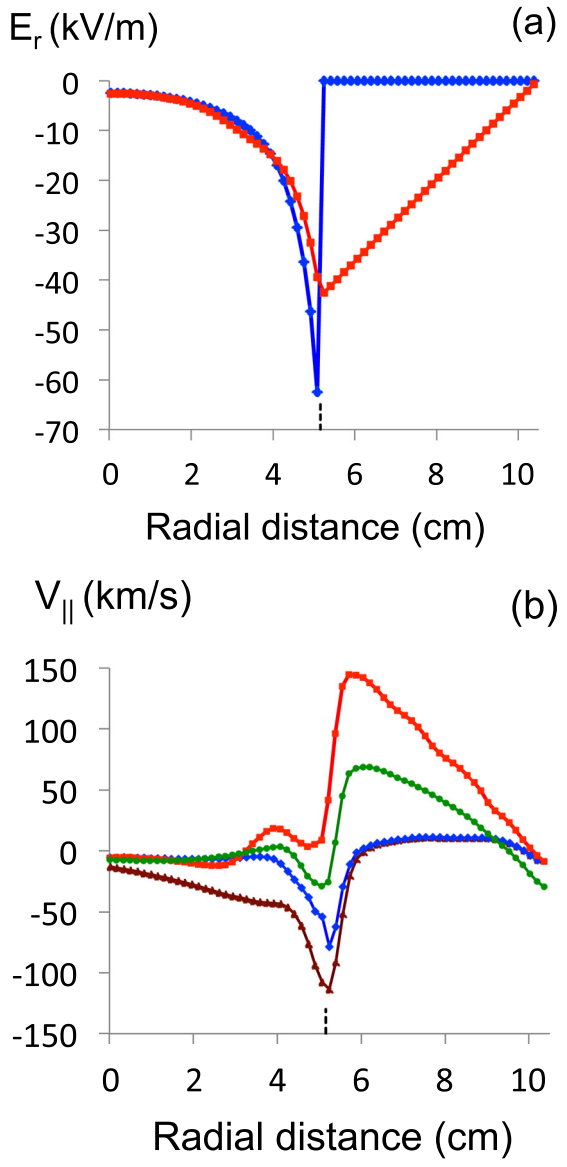

FIG. 8. Collisionless relaxation of a Maxwellian distribution with uniform density and temperature, $T_0 = 1\,\mathrm{keV}$, profiles in the presence of a self-consistent radial electric field [Eq. (10)] obtained for $\bar{B}_\theta = 0.17\,\mathrm{T}$, $I = 0.5\,\mathrm{T\,m}$. Shown are the radial electric field [frame (a)] and the parallel flow velocity [frame (b)] for the cases of the zero (blue diamonds) and extrapolated (red squares) E-field models in the SOL region. Frame (b) also shows the parallel flow velocity obtained for the case of the extrapolated E-field in the SOL region at $t = 0.06\,\mathrm{ms}$ (green circles), and for the case of a zero electric field in the entire simulation domain (brown triangles). Results are evaluated along the outboard midplane and plotted against the radial distance from the inner core boundary. The vertical dashed lines show the location of the separatrix. Except for the data shown by the green circles, all other results are obtained at $t = 0.12\,\mathrm{ms}$. The spatial grid resolution corresponds to $[N_\psi = 32,\ N_\theta = 72]$, $[N_\psi = 32,\ N_\theta = 96]$, and $[N_\psi = 32,\ N_\theta = 24]$ in the CORE, SOL, and PF regions, respectively. The velocity grid is $[N_{v_\parallel} = 72,\ N_\mu = 48]$, and the maximum values of $|v_{||}|$ and μ correspond to $v_\parallel^{max}/V_{T0} = 3.0$, $B_0\mu_{max}/T_0 = 20.0$, where $B_0 = 1.0\,\mathrm{T}$, $V_{T0} = \sqrt{2T_0/m_i}$, and $m_i = 2$. The initial Maxwellian distribution is used to specify the inflow fluxes at the inner radial boundary, and all other boundaries are assumed to absorb particles.

sometimes used in numerical simulations of edge plasmas (e.g., see Ref. 4). This study will help elucidate the discontinuity in the numerical solution for the parallel flow velocity observed at the separatrix for the case of a zero electric field on open field lines [see the blue curve in Fig. 8(b)]. It is hypothesized that the discontinuous feature is related to the instantaneous drop of the electric field to zero across the separatrix, and that the numerical solution should become smoother if continuous extrapolation of E_r into the SOL region is adopted. Note that a radial electric field contributes only to the poloidal and toroidal components of a particle's velocity [see Eq. (2)], and therefore it does not introduce explicit discontinuities in the radial component of the advection velocity. However, a discontinuity in the poloidal velocity can possibly lead to the non-smooth feature observed at the separatrix. We repeat the simulation discussed above by adopting the following model for the radial electric field, E_r, on open field lines: in the SOL region, E_r is linearly extrapolated from its value on the magnetic separatrix to zero at the outer radial boundary; in the PF region E_r is symmetric to its closed-field-line counterpart. Results of the simulations for the radial electric field and ion parallel flow velocity are shown in Fig. 8. It is readily seen that the field magnitude decreases for the case of extrapolated E_r [in Fig. 8(a)], which corresponds to improved confinement of ion orbits. Also, we note that the numerical solution for the parallel flow becomes much smoother at the separatrix. It is interesting that the presence of a strong inward radial E-field on open field lines changes the direction of the parallel flow from co-I_p to counter-I_p. A plausible description of this effect is as follows: Absorbing boundary conditions on the divertor plates lead to the generation of large transient counter-I_p flows in the SOL region. As the transport of the angular momentum becomes significant near the separatrix and can be strongly influenced by a radial electric field, these flows can be transported across the separatrix, thereby changing the flows on closed field lines. To support this argument, the ion parallel flow velocity is shown at the earlier time, $t = 0.06$ ms, which elucidates the change in the parallel flow direction inside the separatrix.

In conclusion, the results shown in Fig. 9 do not correspond to the final quasi-stationary state, and relaxation continues beyond the simulation time of $t_{sim} = 0.12$ ms. The present studies show that achieving the final relaxed state, which include only particles on confined orbits, can be challenging for continuum codes, e.g., COGENT. We observe that there is a small, but finite level of a residual outward radial particle flux even in the absence of any electric fields. Detailed investigations show that the residual level decreases with an increase in the velocity grid resolution. These findings suggest that there may be finite "numerical diffusion" across the steep loss-cone boundaries (i.e., scattering of confined-orbit ions into the loss-cone), which acts as a continuous source of particle losses. However, we note that the edge of a tokamak is distinguished by pronounced collisions, and therefore, the effects of spurious numerical diffusion are typically negligible compared to collisional re-population of loss-cones even for moderate velocity-space resolution.

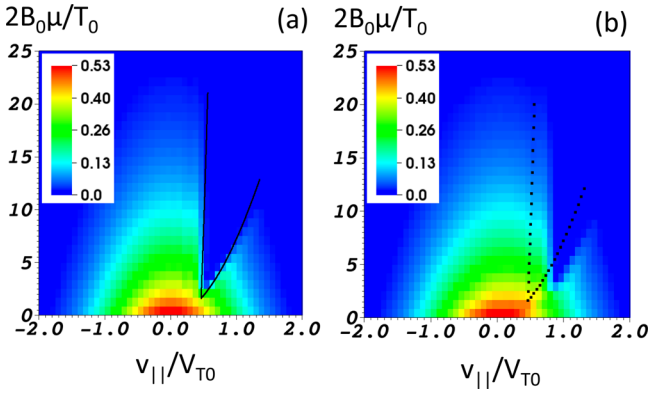

FIG. 9. Collisionless velocity phase-space (in arbitrary units) obtained for the cases of (a) no electric fields and (b) the self-consistent radial electric field given by Eq. (10). The velocity phase-space is computed at the time instant $t = 0.12$ ms at the location $R = 2.08$ m, $Z = 1.76$ m, which corresponds to the point on the outboard midplane, 2.7 cm inside the separatrix. The bold curves in frame (a) and dashed curves in frame (b) show the same analytical solution for the loss-cone boundaries obtained in the absence of electric field [Eq. (8)]. The parameters of the simulation are the same as in Fig. 8.

VI. EFFECTS OF THE ANOMALOUS RADIAL TRANSPORT

As mentioned earlier (see Sec. V), the idealized axisymmetric model that only includes the effects of magnetic drifts and self-consistent radial electric fields predicts steep spatial gradients in the edge region on the order of the inverse ion gyro-radius, $L_p^{-1} \sim \rho_i^{-1}$ (e.g., as analyzed for the parameters of the DIII-D tokamak). This result is inconsistent with abundant experimental data demonstrating much larger length scales for plasma profile variations, ranging from the minor radius, $L_p \sim a$, under the L-mode conditions to the poloidal ion gyro-radius, $L_p \sim \rho_\theta \sim (B_\theta/B_\phi)\rho_i$, for the H-mode conditions.[27] The idealized axisymmetric model, however, omits large contributions to the radial plasma transport produced by microturbulence. While self-consistent description of microturbulence will be addressed with the 5D version of the COGENT code (presently under development), a variety of increasingly detailed model terms have been implemented in the present axisymmetric 4D version to mimic the effects of anomalous radial transport.[28] The presence of strong anomalous diffusion reduces both the plasma spatial gradients and relaxation time, thereby significantly decreasing the computation intensity of edge plasma modeling (cf. Sec. V). For illustrative purposes, results are presented for numerical simulations performed with the parameters characteristic of the DIII-D edge plasma by extending kinetic equation (1) to include a simplified anomalous radial transport model term

$$\frac{\partial B^*_{\|i} f_i}{\partial t} + \nabla_{\mathbf{R}} \cdot \left(\dot{\mathbf{R}}_i B^*_{\|i} f_i \right) + \frac{\partial}{\partial v_\|} \left(\dot{v}_\| B^*_{\|i} f_i \right) = C_i \left[B^*_{\|i} f_i \right] + \frac{1}{J} \frac{\partial}{\partial \psi} \left[\frac{J}{h_\psi^2} D(\psi) \frac{\partial B^*_{\|i} f_i}{\partial \psi} \right]. \quad (13)$$

Here, J is the Jacobian of the coordinate transformation $(R, Z, \phi) \leftrightarrow (\psi, \theta, \phi)$, the radial metric coefficient is given by $h_\psi = \sqrt{(\partial Z/\partial \psi)^2 + (\partial R/\partial \psi)^2}$, and the last term on the

right-hand-side of Eq. (13) represents the "radial" part of the diffusion operator written in a locally orthogonal flux-aligned coordinates (ψ, θ) with the diffusion coefficient D. Note that the radial derivatives are computed in Eq. (13) at fixed $(v_\parallel, \mu)$, and therefore, the radial transport model term does not annihilate a uniform Maxwellian distribution, which typically would be a desired property. The related perturbations, however, are smaller than those driven by the plasma density and temperature gradients by the large factor of $R_0/L_p \gg 1$.

By integrating Eq. (13) over the velocity phase-space and applying the flux-surface average operator, we obtain

$$\frac{\partial \langle n_i \rangle}{\partial t} + \frac{1}{V'}\frac{\partial (\langle \nabla\psi \cdot \mathbf{\Gamma}_i \rangle V')}{\partial \psi} = \frac{1}{V'}\frac{\partial}{\partial \psi}\left[V' \left\langle \frac{|\nabla\psi|}{h_\psi} D(\psi) \frac{\partial n_i}{\partial \psi} \right\rangle \right]. \tag{14}$$

Here, $V = 2\pi \int_0^\psi d\psi \int_0^{2\pi} d\theta J(\psi, \theta)$ is the volume inside a flux surface ψ, $V' = 2\pi \oint J d\theta = \oint\!\!\!\!\!\!\int |\nabla\psi|^{-1} dA$, and dA is the surface element of the magnetic flux surface. Note that the anomalous transport term yields an additional radial ion particle flux. However, we assume that micro-turbulence processes generating anomalous radial transport (e.g., E×B velocity fluctuations) are ambipolar, i.e., they produce the same particle fluxes for both ion and electron species. Therefore, we maintain Eq. (10), which includes only the neoclassical particle fluxes, to describe the self-consistent evolution of a radial electric field. Even with the assumption of "ambipolar microturbulence," the presence of anomalous radial transport can indirectly affect the dynamics of a radial electric field. To illustrate this point, consider a conservation equation for the flux-surface averaged angular momentum in the closed field line region

$$\frac{\partial}{\partial t}\langle L \rangle + \frac{1}{V'}\frac{\partial V' \langle \Pi \rangle}{\partial \psi} = \frac{Z_i e}{c}\langle \nabla\psi \cdot \mathbf{\Gamma}_i \rangle + \left\langle \frac{I}{B}\frac{1}{J}\frac{\partial}{\partial \psi}\left[\frac{J}{h_\psi^2} D(\psi) \frac{\partial}{\partial \psi}\left(\frac{B}{I} L \right) \right] \right\rangle. \tag{15}$$

Here, $L = (I/B) \int dv_\parallel d\mu\, 2\pi B_\parallel^* v_\parallel f_i$ is the toroidal momentum density, $\Pi = (I/B) \int dv_\parallel d\mu\, 2\pi B_\parallel^* v_\parallel f_i (\nabla\psi \cdot \dot{\mathbf{R}}_i)$ represents the stress-tensor term, and the terms on the right-hand-side of Eq. (15) corresponds to the $V_R \times B$ Lorentz force and the anomalous transport of the angular momentum, respectively. First, consider the case where the anomalous transport is not included. Deep in the core region, where deviations from a local Maxwellian distribution are the order of $\Lambda_B/L_p \ll 1$, both the stress-tensor and the radial particle flux terms are very small, which is the consequence of the so-called intrinsic ambipolarity (see, for instance, Ref. 24). As a result, the angular momentum evolves on a long time scale, $\sim \nu_{ii}(\Lambda_B/L_p)^2$, and so does the radial electric field related to the angular momentum via the radial force balance. On the other hand, the presence of the anomalous transport, i.e., the last term on the right-hand-side of Eq. (15), can substantially enhance the relaxation for both the angular momentum and the radial electric field.

Numerical simulations for the parameters characteristic of the DIII-D tokamak are carried out in order to illustrate the effects of anomalous radial transport [see Eq. (13)]. The simulations also include the effects of a self-consistent radial electric field [in Eq. (10)] and the full nonlinear FP ion-ion collisions. Performing computations with the high-order (4-th order) accurate version of COGENT, it was observed that the deviation of the computational grid from the magnetic flux surfaces near the X-point could not be neglected in the implementation of the anomalous transport term in Eq. (13). While this technical detail will be addressed in our future studies, for

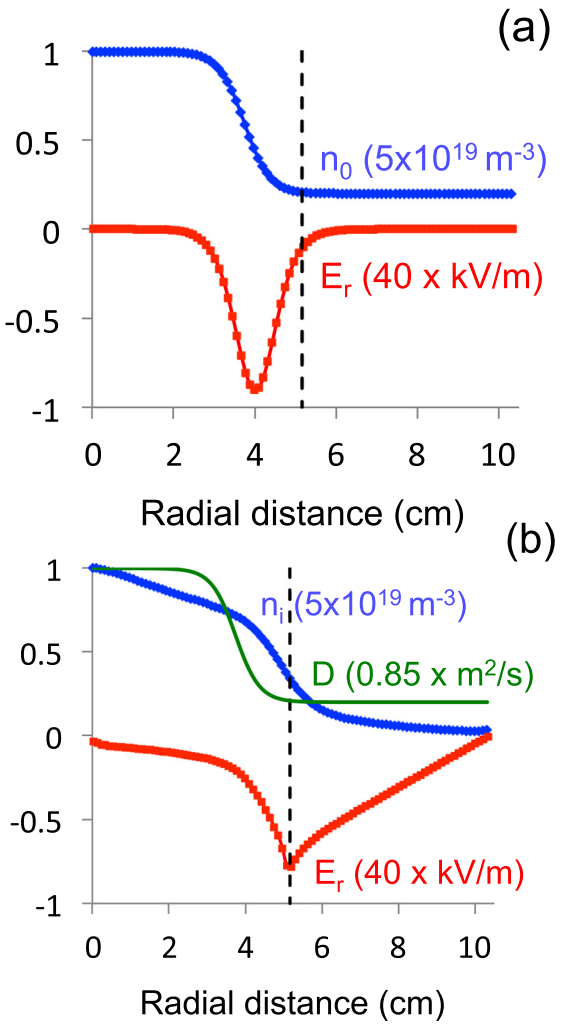

FIG. 10. Relaxation of the edge plasma in the presence of anomalous radial transport, ion-ion collisions, and a self-consistent radial electric filed. Shown are the initial [frame (a)] and final, obtained at $t = 2.6$ ms [frame (b)], profiles of the ion density (blue diamonds) and radial electric field (red squares). The solid green curve in frame (b) illustrates the diffusion coefficient function, $D(\psi)$. Results are obtained along the outboard midplane and plotted against the radial distance from the inner core boundary. The vertical dashed lines show the location of the separatrix. The spatial grid resolution corresponds to $[N_\psi = 48,\ N_\theta = 64]$, $[N_\psi = 48,\ N_\theta = 80]$, and $[N_\psi = 48,\ N_\theta = 16]$ in the CORE, SOL, and PF regions, respectively. The velocity grid is $[N_{v_\parallel} = 48,\ N_\mu = 32]$, and the maximum values of $|v_\parallel|$ and μ correspond to $v_\parallel^{max}/V_{T0} = 3.0$, $B_0\mu_{max}/T_0 = 3.5$, where $B_0 = 1.0$ T, $V_{T0} = \sqrt{2T_0/m_i}$, and $m_i = 2$. The Maxwellian distributions with $n_{BC}^{core} = 5 \times 10^{19}\,\mathrm{m}^{-3}$, $T_0 = 300$ eV and $n_{BC}^{plates} = 0.5 \times 10^{19}\,\mathrm{m}^{-3}$, $T_0 = 300$ eV are used to specify the inflow fluxes at the inner radial boundary and the divertor plates, respectively. The outer SOL and PF radial boundaries are assumed to absorb particles.

the present purposes we circumvent the problem by making use of the lower-order (2nd-order) version of the COGENT code, which employs a locally orthogonal flux-aligned coordinate system in the entire computational domain. The simulations are initialized with the ion distribution function corresponding to a Maxwellian distribution with uniform temperature, $T_0 = 300\,\text{eV}$, zero parallel flow velocity, and the radially varying density profile shown in Fig. 10(a). The same Maxwellian distribution is used to specify inflow fluxes at the inner (CORE) radial boundary. The outer SOL and PF radial boundaries are assumed to absorb particles. To mimic the effect of particle recycling, we specify the inflow fluxes at the divertor plates corresponding to a Maxwellian distribution with $n_{BC} = 0.5 \times 10^{19}\,\text{m}^{-3}$ and $T_{BC} = 300\,\text{eV}$. The initial radial electric field corresponds to the Boltzmann equilibrium i.e., $Z_i e n_0(\partial\Phi_0/\partial\psi) = -T_0(\partial n_0/\partial\psi)$. The subsequent evolution of the electric field is given by Eq. (10) on closed field lines, and on open field lines the electric field perturbation (from the initial distribution) is linearly extrapolated from its value on the separatix to zero at the outer radial boundary. Due to the presence of strong anomalous transport $D \sim 1\,\text{m}^2/\text{s}$ [see Fig. 10(a) for details of the $D(\psi)$ function], the system relaxes to the final state illustrated in Fig. 10 within a characteristic time period of $\tau_{rel} \approx 2.6\,\text{ms}$. Note that the pedestal structure and a radial length scale for variations in plasma parameters, $L_p \sim 1\,\text{cm}$, are roughly consistent with those of the DIII-D pedestal under the H-mode conditions (e.g., see Refs. 15 and 27).

VII. CONCLUSIONS

In this paper, we present the first 4D (axisymmetric) high-order continuum drift-kinetic transport simulations that span the magnetic separatrix of a tokamak. The calculations include fully nonlinear Fokker-Plank collisions, self-consistent electrostatic potential variations, and the model effects of anomalous radial transport. The code, COGENT, is distinguished by a fourth-order finite-volume discretization combined with mapped multiblock grid technology to handle the strong anisotropy of plasma transport and the complex magnetic X-point divertor geometry with high accuracy.

The code is successfully verified against analytical calculations for the case of collisionless relaxation of an ion species in the tokamak edge region in the absence of electric fields. The appearance of loss-cone regions and the associated co-I_p toroidal rotation at the outboard midplane are observed. The collisional repopulation of the loss-cone regions is then analyzed for the parameters characteristic of the DIII-D tokamak. It is found that deviations from a local Maxwellian distribution can be significant, especially in the loss cone regions, and the full nonlinear Fokker-Planck collision model may be required for accurate edge plasma modeling. The effects of self-consistent potential variations are presently included via a simplified flux-surface average balance equation for the ion polarization and neoclassical currents. This electric field model neglects poloidal variations in the electrostatic potential and adopts *ad-hoc* specifications of the radial electric field in the open field line regions. Generation of a strong radial electric field, along with mitigation of the ion orbit loss and parallel flows, is observed. Finally, the effects of anomalous transport are addressed by including a simple radial diffusion term into the gyro-kinetic equation, and an illustrative steady-state solution is obtained for the parameters characteristic of the DIII-D tokamak.

The present work discusses the initial proof-of-principle simulations of axisymmetric cross-separatrix kinetic plasma transport. Although providing important insights into the dynamics of edge plasmas, the present modeling omits several important physical phenomena. These include, for instance, the effects of poloidal variations in the electrostatic potential, near-boundary (sheath) physics at the divertor plates, kinetic electrons, neutrals, and impurities. Our future work will extend the analysis to incorporate these effects.

ACKNOWLEDGMENTS

The authors gratefully acknowledge our collaborators in the Applied Numerical Algorithms Group at Lawrence Berkeley National Laboratory (LBNL) for the their assistance in the development of the numerical algorithms and software infrastructure underlying the COGENT code. We are also grateful to Gunther Weber of LBNL for his expert services in implementation of the visualization tool VisIt. This research was supported by the U.S. DOE, Office of Science, Fusion Energy Sciences under Contract No. DE-AC52-07NA27344.

[1]J. Candy and R. E. Waltz, Phys. Rev. Lett. **91**, 045001 (2003).
[2]F. Jenco, W. Dorland, M. Kotschenreuther, and B. N. Rogers, Phys. Plasmas **7**, 1904 (2000).
[3]C. S. Chang, S. Ku, and H. Weitzner, Phys. Plasmas **11**, 2649 (2004).
[4]D. J. Battaglia, C. S. Chang, S. M. Kaye, K. Kim, S. Ku, R. Maingi, R. E. Bell, A. Diallo, S. Gerhardt, B. P. LeBlanc, J. Menard, M. Podesta, and NSTX Team, Nucl. Fusion **53**, 113032 (2013).
[5]D. J. Battaglia, K. H. Burrell, C. S. Chang, S. Ku, J. S. deGrassie, and B. A. Grierson, Phys. Plasmas **21**, 072508 (2014).
[6]T. Takizuka, Plasma Sci. Technol. **13**, 316 (2011).
[7]P. Colella, M. R. Dorr, J. A. F. Hittinger, and D. F. Martin, J. Comput. Phys. **230**, 2952 (2011).
[8]M. R. Dorr, R. H. Cohen, P. Colella, M. A. Dorf, J. A. F. Hittinger, and D. F. Martin, in Proceedings of the SciDAC 2010 Conference, Tennessee (2010).
[9]P. McCorquodale, M. R. Dorr, J. A. F. Hittinger, and P. Colella, J. Comput. Phys. **288**, 181 (2015).
[10]M. A. Dorf, R. H. Cohen, J. C. Compton, M. Dorr, T. D. Rognlien, J. Angus, S. Krasheninnikov, P. Colella, D. Martin, and P. McCorquodale, Contrib. Plasma Phys. **52**, 518 (2012).
[11]M. A. Dorf, R. H. Cohen, M. Dorr, J. Hittinger, and T. D. Rognlien, Contrib. Plasma Phys. **54**, 517 (2014).
[12]M. A. Dorf, R. H. Cohen, M. Dorr, T. Rognlien, J. Hittinger, J. Compton, P. Colella, D. Martin, and P. McCorquodale, Phys. Plasmas **20**, 012513 (2013).
[13]M. A. Dorf, R. H. Cohen, M. Dorr, T. Rognlien, J. Hittinger, J. Compton, P. Colella, D. Martin, and P. McCorquodale, Nucl. Fusion **53**, 063015 (2013).
[14]J. E. Rice, A. Ince-Cushman, J. S. deGrassie, L.-G. Eriksson, Y. Sakamoto, A. Scarabosio, A. Bortolon, K. H. Burrell, B. P. Duval, C. Fenzi-Bonizec, M. J. Greenwald, R. J. Groebner, G. T. Hoang, Y. Koide, E. S. Marmar, A. Pochelon, and Y. Podpaly, Nucl. Fusion **47**, 1618 (2007).
[15]J. S. deGrassie, R. J. Groebner, K. H. Burrell, and W. M. Solomon, Nucl. Fusion **49**, 085020 (2009).
[16]S. C. Chang and S. Ku, Phys. Plasmas **15**, 062510 (2008).
[17]X. Q. Xu, K. Bodi, R. H. Cohen, S. Krasheninnikov, and T. D. Rognlien, Nucl. Fusion **50**, 064003 (2010).
[18]T. S. Hahm, Phys. Plasmas **3**, 4658 (1996).
[19]R. L. Miller, M. S. Chu, J. M. Greene, Y. R. Lin-Liu, and R. E. Waltz, Phys. Plasmas **5**, 973 (1998).
[20]See https://nersc.gov for National energy research scientific computing center.

[21]J. D. Huba, *NRL Plasma Formulary (NRL/PU/6790-94-265)* (Naval Research Laboratory, 1994).
[22]W. X. Wang, F. L. Hinton, and S. K. Wong, Phys. Rev. Lett. **87**, 055002 (2001).
[23]F. I. Parra and P. J. Catto, Plasma Phys. Controlled Fusion **50**, 065014 (2008).
[24]M. A. Dorf, R. H. Cohen, A. N. Simakov, and I. Joseph, Phys. Plasmas **20**, 082515 (2013).
[25]P. C. Stangeby, *The Plasma Boundary of Magnetic Fusion Devices* (IoP Publishing Ltd., Bristol, 2000).
[26]G. Kagan and P. Catto, Plasma Phys. Controlled Fusion **52**, 055004 (2010).
[27]A. W. Leonard, Phys. Plasmas **21**, 090501 (2014).
[28]J. Angus, "On anomalous plasma transport in the edge of magnetic confinement devices," Ph.D. thesis, University of California, San Diego, 2012.